Research Article Vol. 7, No. 8 / August 2020 / Optica 973

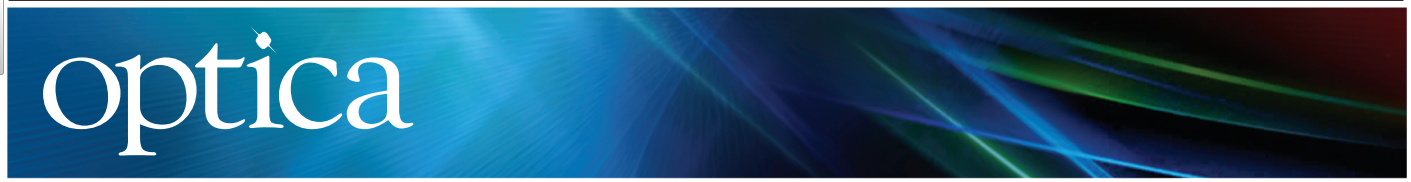

Tunable SIM: observation at varying spatiotemporal resolutions across the FOV

Taeseong Woo,[1] Su Hyun Jung,[1] Cheolwoo Ahn,[1] Byungjae Hwang,[1] Hyunggee Kim,[2] Joo H. Kang,[1] and Jung-Hoon Park[1,*]

[1]Department of Biomedical Engineering, Ulsan National Institute of Science and Technology (UNIST), Ulsan 44919, South Korea
[2]Department of Biotechnology, College of Life Sciences and Biotechnology, Korea University, Seoul 02841, South Korea
*Corresponding author: jh.park@unist.ac.kr

Received 13 March 2020; revised 9 June 2020; accepted 8 July 2020 (Doc. ID 392800); published 10 August 2020

To date, imaging systems have generally been designed to provide an even spatiotemporal resolution across the field of view (FOV). However, this becomes a fundamental limitation when we aim to simultaneously observe varying dynamics at different parts of the FOV. In conventional imaging systems, to capture fast dynamics occurring at only a small portion of the FOV, the entire imaging system's sampling rate must be increased. This is a major problem if different parts of the FOV must rather be imaged at high spatial resolutions beyond the diffraction limit and require a sacrifice in temporal resolution. To answer this unmet challenge, we propose tunable SIM, which enables adaptive modulation of spatiotemporally varying structured illumination across different parts of the FOV. Using tunable SIM, we exploit the varying and designable spatiotemporal resolution to demonstrate simultaneous measurements of subdiffraction-limited changes in the actin fine structure of U87MG-EGFP-CD9 cells and the fast viscous flow inducing these structural changes.

https://doi.org/10.1364/OPTICA.392800

1. INTRODUCTION

Recent development of fluorescence based super-resolution (SR) microscopy techniques have opened a new era of biological imaging at subcellular and even molecular scales, which could not be dreamed of when using conventional diffraction-limited microscopes [1–5]. Due to their large impact on the field, various SR methods, such as single molecule localization microscopy (SMLM) [6,7], stimulated emission depletion (STED) [8,9], and structured illumination microscopy (SIM) [10–14] have been successfully commercialized despite their relatively short history. However, one of the major drawbacks of SR imaging is the fact that temporal resolution must be sacrificed for the spatial resolution enhancement. Because the characteristic scales of spatial structure and temporal dynamics can vary widely across the FOV, an imaging system that can actively change the spatiotemporal resolution across the FOV can potentially benefit from both the high spatial resolution of SR imaging and the fast temporal resolution of conventional widefield imaging.

All SR methods are based on some type of spatial or temporal modulation on the fluorescence signal which decreases the temporal resolution. SMLM depends on repeated measurements of stochastic fluorescent signals, and, therefore, the method cannot arbitrarily obtain fast diffraction-limited images for selected parts of the FOV if needed. The full image sequence for SMLM must still be collected and summed to obtain a single conventional diffraction-limited image. This limitation is similar for STED as well. Although the imaging speed can fundamentally be similar to conventional diffraction-limited confocal microscope systems, the increased resolution requires higher spatial sampling resulting in a decrease in temporal resolution for the same FOV. To increase the framerate, laser scanning based SR systems can be easily transitioned to a diffraction-limited system by simply converting the laser beam to a standard diffraction-limited focus. However, because the framerate for a laser scanning microscope is affected by the sequential sum of all sampling points over the FOV, there is no trivial method to arbitrarily change the temporal resolution simultaneously for different parts of the FOV.

Among the SR variants, SIM stands out in terms of temporal resolution. SIM uses standard fluorescent probes and illuminates the entire FOV simultaneously which is crucial for fast imaging. Based on such characteristics, SIM is currently one of the methods of choice for the everyday biologist because of low phototoxicity and high speed. This enables fast live imaging over extended periods of time which often becomes the deciding factor despite the resolution being limited to only twice the diffraction limit (~100 nm for visible light). On the other hand, although SIM is faster than SMLM or STED by more than 10-fold when imaging the same FOV [12,15–17], SIM is still 9 or 15 times slower (for 2D, 3D-SIM, respectively) than conventional widefield imaging. In short, simultaneous measurement of different areas of the FOV at different spatiotemporal resolutions is not yet possible using current SR techniques.

Corrected 12 August 2020

To answer this unmet need, we propose tunable SIM, which enables adaptive modulation of spatiotemporally varying structured illumination across different parts of the FOV. Using tunable SIM, we demonstrate simultaneous measurements of subdiffraction-limited changes in the actin fine structure of U87MG-EGFP-CD9 (U87) cells and the fast viscous flow surrounding the cells. Tunable SIM combines the best of SIM and conventional widefield imaging to enable adaptive observation at varying spatial resolutions across the FOV.

2. METHODS

A. Tunable SIM

By illuminating the sample with a pattern of light with uneven intensity, we obtain a fluorescent image expressed as

$$I(\boldsymbol{r}) = \{O(\boldsymbol{r}) \cdot P(\boldsymbol{r})\} * \mathrm{PSF}, \tag{1}$$

where $O(\boldsymbol{r})$ is the object of interest, $P(\boldsymbol{r})$ is the patterned structured illumination, and PSF is the point spread function of the optical system, respectively. SIM typically uses sinusoidal illumination patterns to obtain higher spatial frequency contents surpassing the diffraction limit. By utilizing sinusoidal illumination patterns with periods at the diffraction limit, lateral resolution of linear SIM can be enhanced along the vertical direction of the illumination fringes by two-fold. As the resolution enhancement is directional, three different angles of sinusoidal illumination are typically used to obtain isotropic resolution enhancement. In addition, because the sinusoidal illumination on the sample manifests as three overlapped convolution terms in Fourier space, at least three measurements are needed for each illumination angle to decipher the overlapped information. For 3D-SIM, three-beam interference results in five overlapping terms in Fourier space which requires five measurements per illumination angle for the corresponding information retrieval.

Due to the additional information collection, although SIM is the fastest SR method to date, it is still 9–15 times slower than conventional widefield imaging. Although we can use a part of the acquired SIM images to reconstruct a widefield image, the reconstruction requires three or five images (for 2D and 3D-SIM, respectively) which still suffers from temporal resolution loss. Various SIM methods have been developed to decrease acquisition time [12,15,18–24], but they all still need to acquire multiple images which is the fundamental requirement for SIM [25–27]. Because the reconstruction is only valid for objects that do not move or change during each image acquisition sequence, severe artifacts can be seen in SIM image reconstruction of dynamic objects [28–30].

Fortunately, for many real-life scenarios, the temporal dynamics vary widely across the FOV. Exploiting this property, we can divide the objects of interest into different regions as follows:

$$O(\boldsymbol{r}, t) = O(\boldsymbol{r}_s) + O(\boldsymbol{r}_d, t), \tag{2}$$

where $O(\boldsymbol{r}_s)$ represents slowly changing object areas that can be considered as stationary with respect to a single SIM illumination sequence. On the other hand, $O(\boldsymbol{r}_d, t)$ corresponds to dynamic regions where the change is much faster than a single SIM illumination sequence time. By modulating the illumination pattern in a spatially inhomogeneous manner, the patterned structured illumination can also be separated into two terms,

$$P(\boldsymbol{r}, t) = P_{\mathrm{SIM}}(\boldsymbol{r}_s, t) + P_{\mathrm{WF}}(\boldsymbol{r}_d), \tag{3}$$

where $P_{\mathrm{SIM}}(\boldsymbol{r}_s, t)$ and $P_{\mathrm{WF}}(\boldsymbol{r}_d)$ correspond to a sinusoidal SIM illumination pattern sequence and homogeneous plane illumination for the stationary and dynamic regions, respectively. By substituting Eqs. (2) and (3) into Eq. (1), we obtain,

$$\begin{aligned} I(\boldsymbol{r}, t) &= [\{O(\boldsymbol{r}_s) + O(\boldsymbol{r}_d, t)\} \cdot \{P_{\mathrm{SIM}}(\boldsymbol{r}_s, t) + P_{\mathrm{WF}}(\boldsymbol{r}_d)\}] * \mathrm{PSF} \\ &= \{O(\boldsymbol{r}_s) \cdot P_{\mathrm{SIM}}(\boldsymbol{r}_s, t) + O(\boldsymbol{r}_d, t) \cdot P_{\mathrm{WF}}(\boldsymbol{r}_d)\} * \mathrm{PSF}. \end{aligned} \tag{4}$$

We see that the SIM image reconstruction can now be specifically applied upon target selected regions $\boldsymbol{r}_s$ that can be considered stationary for an entire SIM illumination sequence. In doing so, the reconstructed super-resolved image is no longer corrupted by movement induced artifacts. The dynamic regions $\boldsymbol{r}_d$ can now be independently observed to track dynamic processes faster than the SIM acquisition speed, albeit at diffraction-limited resolution. Therefore, by segmenting the illumination with respect to temporal characteristics of the objects of interest, we realize a unique imaging system that has varying spatiotemporal resolutions across the FOV that can be tunable to the user's needs. Furthermore, as the illumination pattern can be changed arbitrarily without any moving mechanical parts, the stationary and dynamic regions $\boldsymbol{r}_s$ and $\boldsymbol{r}_d$ can adaptively change to track arbitrary objects of interest. We also emphasize that in this work, the term "stationary" stands for stationary with respect to a single SIM sequence. Dynamics within the SIM temporal resolution can also be tracked in the stationary regions as well.

The concept of tunable SIM is shown in Fig. 1. Figure 1(a) shows a representative time-lapse of cells with complex subcellular structures surrounded by flowing fluorescent beads. The cells have subcellular structures that cannot be resolved with diffraction-limited resolution. In the simulation, we assume that the cells do not move or change shape during a single 3D-SIM acquisition sequence. The flowing beads, on the other hand, change position at every time point. In conventional microscopes, we would have to resort to diffraction-limited widefield imaging shown in Fig. 1(b) to prevent motion artifacts and capture the full dynamics. In this case, the flowing beads can be tracked at the cost of a loss in SR imaging of subcellular processes in the cells [Fig. 1(e)]. On the other hand, if we perform conventional SIM, the flowing beads cannot be tracked or imaged to any detail [Figs. 1(c) and 1(f)]. In addition, the dynamics of the flowing beads also induces artifacts in the SIM reconstruction as well. Although subcellular structures deep within the cell can be imaged at subdiffraction-limited resolution via SIM reconstruction, important dynamics of the outer cytoskeletal structure near the cell membrane interacting with the time-varying environment cannot be imaged due to motion artifacts (see Fig. S1 of Supplement 1). In tunable SIM, SIM illumination patterns can be selectively applied to the cell-specific regions as shown in Fig. 1(d). These selected regions need not be continuous, and their shape can be perfectly adapted to match the areas that must be observed at higher spatial resolution. The rest of the FOV is illuminated with a homogeneous plane wave that allows imaging at 15-fold temporal resolution with respect to SIM. By combining the advantages of widefield imaging and SIM, spatially varying spatiotemporal resolution can be achieved to simultaneously observe varying dynamics in space and time across different parts of the FOV as shown in Fig. 1(g). Due to the independent illumination and reconstruction for the different

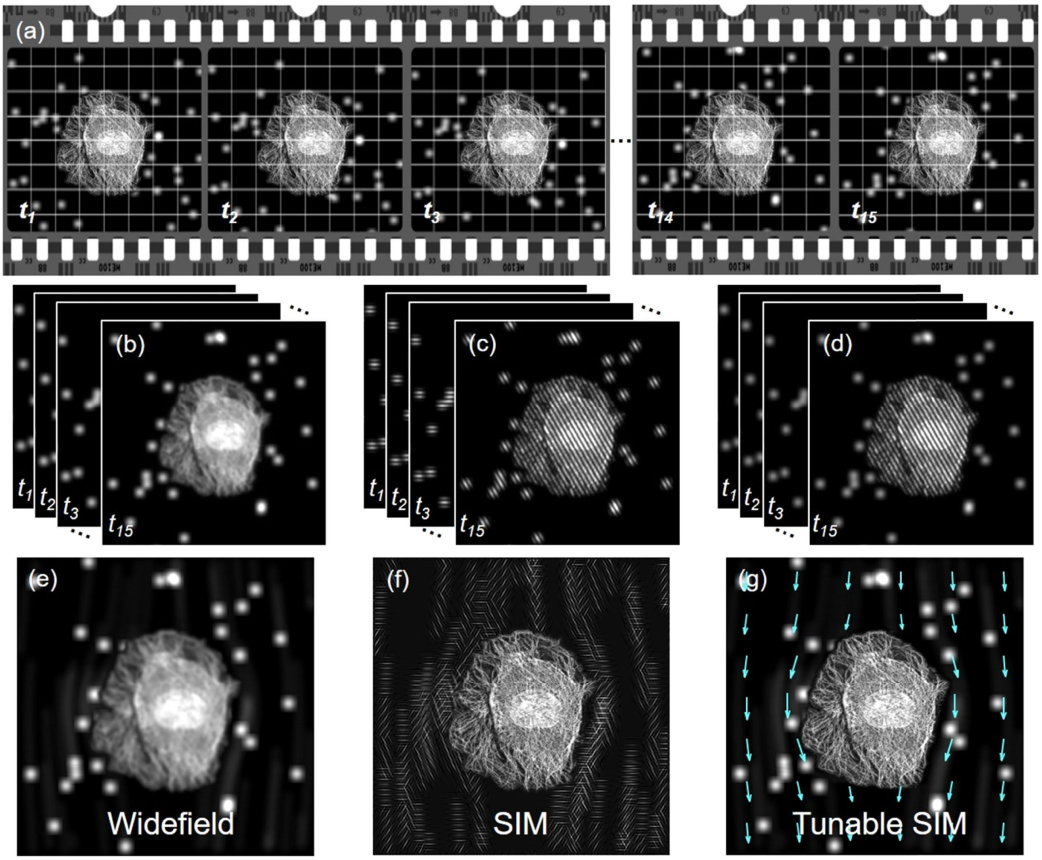

Fig. 1. Schematic of tunable SIM. (a) Simulation model containing both subcellular fine structure and time-varying objects in a single time sequence ($t_1 - t_{15}$). Gridlines are guides to the eye to show the uneven flow of beads. Simulated data acquired under different illumination conditions; (b) widefield, (c) SIM, and (d) tunable SIM, respectively. Reconstructed (e) widefield, (f) SIM, and (g) tunable SIM images. Widefield imaging misses SR imaging of subcellular fine structure, while SIM fails to track dynamic objects. Tunable SIM can arbitrarily obtain full temporal resolution or subdiffraction-limited resolution at different areas of the FOV to successfully image the subcellular structures and fast surrounding flow simultaneously. The fluid flow velocity map in Fig. 1(g) was generated by combining 15 images obtained at different time points ($t_1 - t_{15}$).

areas, SIM reconstruction at targeted areas is not compromised by nearby dynamic changes.

B. Experimental Setup

The experimental setup for tunable SIM is schematically represented in Fig. 2. A circularly polarized plane wave was sent to the DMD (DLP LightCrafter 6500, Texas Instruments) to generate a constant modulation depth for the 3D-SIM patterns, regardless of their orientation angle. If perfect modulation depth is required, the three beams should maintain s-polarization for all orientation angles which requires additional hardware and synchronization of adjustable waveplates. A simpler option to increase the modulation depth, although not perfect in this case, would be to use a segmented azimuthal polarizer that filters just the first order beams to s-polarization, while the zeroth order beam maintains circular polarization (see Fig. S3 of Supplement 1 for details on modulation depth per polarization). This option does not require any moving parts or synchronization and will not harm the imaging speed of the system. The DMD modulates the incident light dynamically with binary patterns to generate tunable SIM illumination patterns, adaptive to time-varying objects. Using acquired images as real-time feedback, the stationary $\boldsymbol{r}_s$ and dynamic $\boldsymbol{r}_d$ regions were automatically segmented based on movement between image frames as shown in Fig. 3. High-order diffraction beams due to discrete DMD pixels were blocked by a custom binary mask made with anodized aluminum foil placed on a Fourier conjugate plane. By passing only the first and zeroth diffraction orders through the mask, binary patterns on the DMD were bandpass filtered to simultaneously obtain spatially varying analog 3D-SIM and homogeneous illumination on the stationary $\boldsymbol{r}_s$ and dynamic regions $\boldsymbol{r}_d$, respectively. The pixels of the DMD and sCMOS camera (Zyla 4.2, Andor) were matched pixel by pixel to apply the appropriate tunable SIM illumination to correct locations of the FOV (see Fig. S4 of Supplement 1). To maximize the observable FOV while satisfying the Nyquist limit, the DMD was demagnified by 88.8 times so that 2.5 pixels of the DMD corresponded to the diffraction limit (210 nm for excitation) defined by the numerical aperture of the objective lens (1.4 NA, 100×, oil immersion, OLYMPUS). The peak wavelengths for excitation, and emission were 488 and 525 nm, respectively. To minimize wavefront distortion and depolarization, we employed a 3 mm thick ultraflat dichroic mirror (ZT488rdc-UF3, Chroma) equipped in a custom cube (91044, Chroma). The DMD, camera, and laser were synchronized using a TTL signal from the DMD as the master clock for fast image acquisition without crosstalk from delays between different hardware components (see Fig. S5 of Supplement 1 for details of image acquisition sequence).

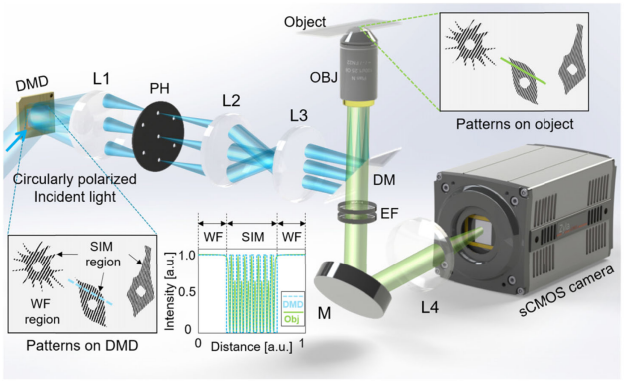

Fig. 2. Experimental setup. Incident light is modulated by binary patterns on a DMD. By selecting the first and zeroth diffraction orders using a custom pinhole, tunable SIM patterns with simultaneous sinusoidal 3D-SIM and widefield illumination at arbitrary regions are obtained (see Fig. S2 of Supplement 1 for details of illumination pattern generation). Inset: Blue lines show the binary patterns displayed on the DMD, green lines show the resulting filtered 3D SIM patterns on the object. DMD, digital micromirror device; L1-L4, lenses ($f_1 = 400$, $f_2 = 750$, $f_3 = 300$, $f_4 = 180$ mm); PH, pinhole; OBJ, objective lens; DM, dichroic mirror; EF, emission filter; M, mirror.

C. Operation

The operation flow chart for tunable SIM is shown in Fig. 3. The tunable SIM patterns that realize the correct spatially varying spatiotemporal resolutions were obtained automatically using the acquired images. To start the process, the initial acquisition was carried out by applying conventional SIM patterns onto the entire FOV. Taking the first two SIM images, we applied Gaussian, top-hat filters, and additional morphological image processing to binarize the images (see Fig. S6 of Supplement 1 for details on tunable SIM pattern sequence generation). Assuming time-varying objects exist at different locations in each image, we can differentiate the stationary $\boldsymbol{r}_s$ and dynamic regions $\boldsymbol{r}_d$ by performing an AND operation on the binary image pair. The relatively slowly changing regions which are appropriate for structured illumination and SIM reconstruction can be directly identified, while the rest of the FOV maximizes their temporal resolution using homogeneous plane wave illumination. By modulating the DMD adaptively in a single image, arbitrary structured illumination patterns could be displayed in different parts of the FOV simultaneously [26,31,32]. After the generation of the appropriate tunable SIM pattern, a tunable SIM illumination sequence was measured. Thereafter, the tunable SIM illumination sequence pattern was continuously renewed to dynamically follow time-varying location and shape of the biological samples. The adaptive tunable SIM illumination pattern calculation was carried out repeatedly by employing the last two images acquired in the previous tunable SIM pattern sequence for the segmentation of the stationary $\boldsymbol{r}_s$ and dynamic regions $\boldsymbol{r}_d$ for the next measurement sequence and enabled continuous tracking of the cell body.

To enable seamless tracking of live dynamics, we implemented the tunable SIM illumination pattern mask calculation in real-time based on parallel computation. We used MATLAB 2017b for computing the illumination patterns, sending the tunable SIM patterns to the DMD, and acquiring images, simultaneously. Psychtoolbox [33] was used to refresh tunable SIM patterns on the DMD at a fixed repetition rate. However, we found that Psychtoolbox is sensitive to delays induced by other computation processes that were performed in the background of the same Matlab session. To solve this issue, we divided the computation and hardware command steps such that the tunable SIM illumination commands using Psychtoolbox and the image acquisition and processing steps were performed on two different MATLAB sessions. In this process, we utilized the Sharedmatrix toolbox [34] to send the computed tunable SIM illumination patterns to Psychtoolbox running on the other MATLAB session. By parallelizing the illumination, image acquisition, and tunable SIM pattern calculation steps, seamless image acquisition was realized. The final SIM image reconstruction process for the SR resolved regions was performed using the fairSIM plugin in ImageJ [35,36] (see Figs. S7–S9 of Supplement 1 for details of tunable SIM image reconstruction). Our current implementation performs the data acquisition, calculation, and DMD control all through the Matlab platform which poses an upper limit on optimization. Future upgrades, for instance, by

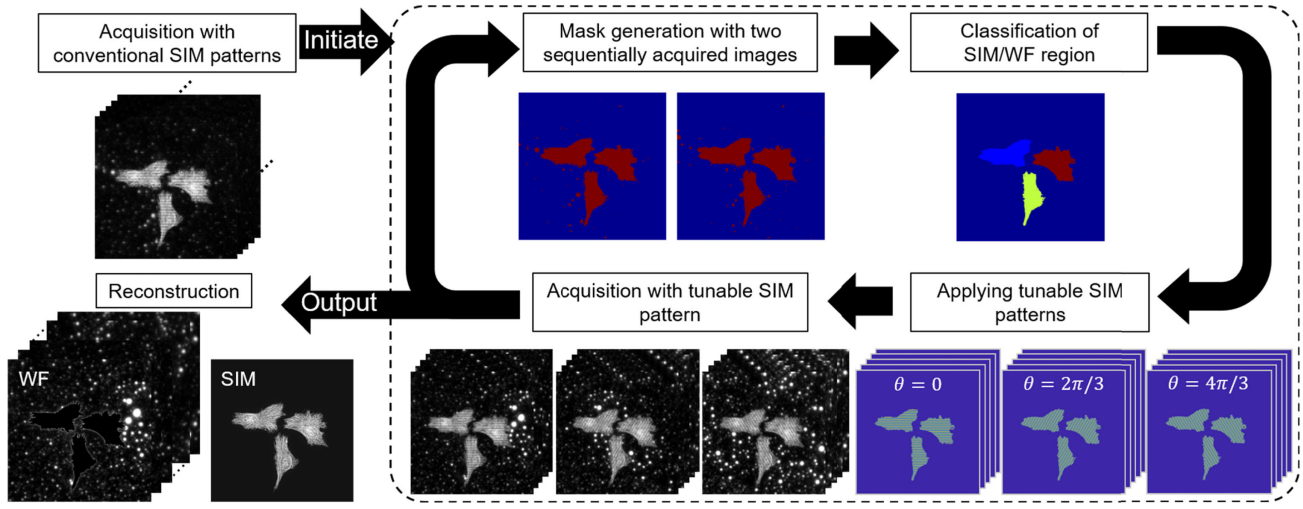

Fig. 3. Tunable SIM flowchart. Image acquisition was initiated by applying conventional SIM patterns to the entire FOV, the first two images were used to make a binary image pair for region identification. Dynamic object regions were identified by performing an AND operation on the image pair. Tunable SIM illumination patterns were generated using the classification of dynamic and stationary regions. The acquired tunable SIM images were used for sequent tunable SIM pattern updates.

utilizing custom DMD-firmware and FPGA based computation, can potentially enable the synergistic utilization of the full speed of both DMDs and fast sCMOS cameras.

3. RESULTS

To quantify the spatial resolution of our tunable SIM system, we carried out imaging experiments with 100 nm diameter fluorescent nanobeads (FCDG002, Bangs Laboratories). The results for conventional widefield imaging, Wiener deconvolution, and SIM images are shown in Figs. 4(a)–4(c), respectively. Widefield imaging was simply performed by turning on all DMD pixels. The SIM image was obtained by applying the appropriate 2D gratings over the entire DMD as demonstrated in previous works. The image resolution was quantified by averaging the intensity full width at half maximum (FWHM) of 20 random beads in each image as shown in Fig. 4(f). As expected, we obtained a FWHM of 101 ± 7.9 nm for the SIM image demonstrating that resolution doubling was well obtained in our DMD based SIM system, compared with theoretical and measured diffraction-limited resolution of 229 and 243.3 ± 14.8 nm, respectively. See Fig. S10 of Supplement 1 for further verification using a resolution ruler target (SIM 140B, GATTA-quant).

We next performed tunable SIM on the same sample to verify that varying image resolutions can be obtained in arbitrary regions of the FOV. We designed the tunable SIM illumination pattern to double the resolution in only the areas within the boundaries of the letters "UNIST" [Fig. 4(d)]. All DMD pixels were well matched pixel by pixel to the camera to realize easy and accurate targeted custom structured illuminations. The obtained resolution in the different targeted areas also agreed with the results obtained using conventional methods verifying that selective SIM illumination

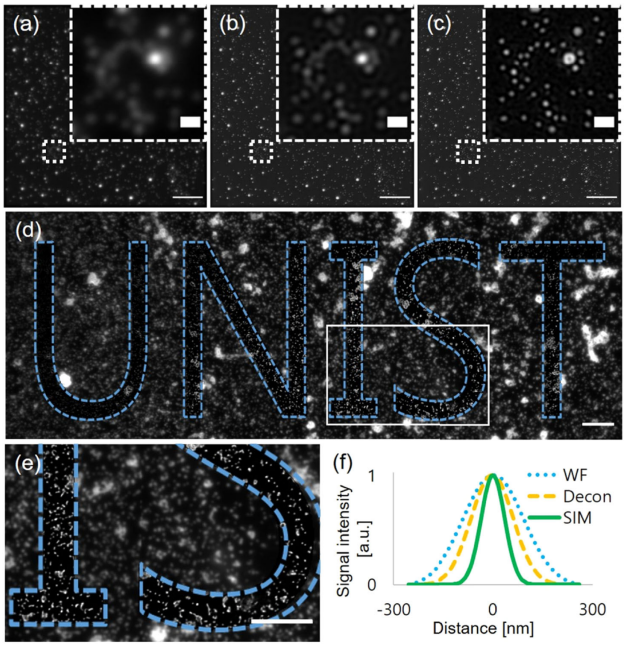

Fig. 4. 100 nm diameter nanobeads imaged by (a) widefield, (b) Wiener deconvolution, and (c) SIM. (d) Tunable SIM images of nanobeads with SR applied only to the areas bounded by the letters 'UNIST', and (e) a magnified subarea outlined by a white solid square in (d). (f) Averaged intensity plot of 20 random beads. Scale bars; 5 μm. 0.5 μm in insets of (a–c).

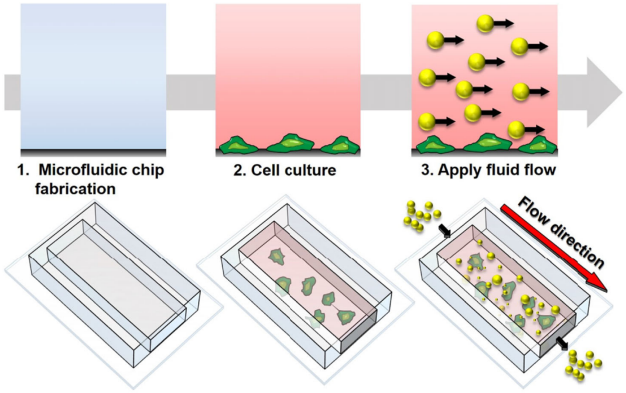

Fig. 5. Sample preparation. Cuboid shaped microfluidic chip was fabricated with polydimethylsiloxane (PDMS). U87MG-EGFP-CD9 cells were cultured in the channel for 72 h. Fluorescent beads were introduced into the channel with a constant pressure (2 μl/min) using a syringe pump.

and reconstruction can be directly applied without any resolution loss.

Using tunable SIM, we next imaged dynamics at different scales in both space and time. By culturing U87 cells in a microfluidic channel (3 mm width × 20 μm height), we controlled the flow of the surrounding medium to induce shear stress related response on the U87 cells as shown in Fig. 5. By diluting 1 μm fluorescent beads (FCM-1052-2, Spherotech, Inc.) in the medium, we performed simultaneous measurements of the subdiffraction-limited changes of the subcellular actin cytoskeletal structure as well as the fast fluid flow velocity distribution directly surrounding and influencing the cells. Using a syringe pump (Fusion 200, Chemyx, Inc.), we applied an input flow of 2 μl/min to obtain a maximum flow velocity of approximately 830 μm/s based on the width and height of the channel. Using conventional SIM, the moving beads and thus the flow velocity distribution could not be observed due to motion artifacts. To visualize the flow, conventional methods would have to resort to diffraction-limited widefield imaging at the cost of losing subdiffraction-limited resolution imaging of the actin fine structure. In contrast, by applying tunable SIM, the bead flow was visualized at the full frame rate of the image acquisition at 30 Hz, while the actin fine structure of the U87 cells were reconstructed using 3D-SIM resulting in image acquisition at 6 Hz (using rolling reconstruction sequences, e.g., frames 1–15, 6–20, 11−25 …, [15,37]) but at twice the resolution.

Using tunable SIM, we exploited the higher temporal resolution in visualizing the extracellular environment to analyze the fluid stream surrounding the cell. The segmentation process for bead flow visualization is shown in Fig. 6. First, tunable SIM illumination pattern sequences were applied onto the sample to obtain images with spatially varying spatiotemporal resolutions. In this work, the liquid flow was still faster than the exposure time of our camera; therefore, the beads were captured as ellipsoidal-shapes as shown in Fig. 6(a), due to their movement within a single exposure. We averaged all acquired images then subtracted the averaged image from each raw data frame in the $\boldsymbol{r}_d$ regions to remove stationary objects such as debris and adhered beads in the microfluidic channel. Through this simple procedure, we obtained only the moving beads in the $\boldsymbol{r}_d$ regions of each frame. However, some beads can flow over the cell and travel through both

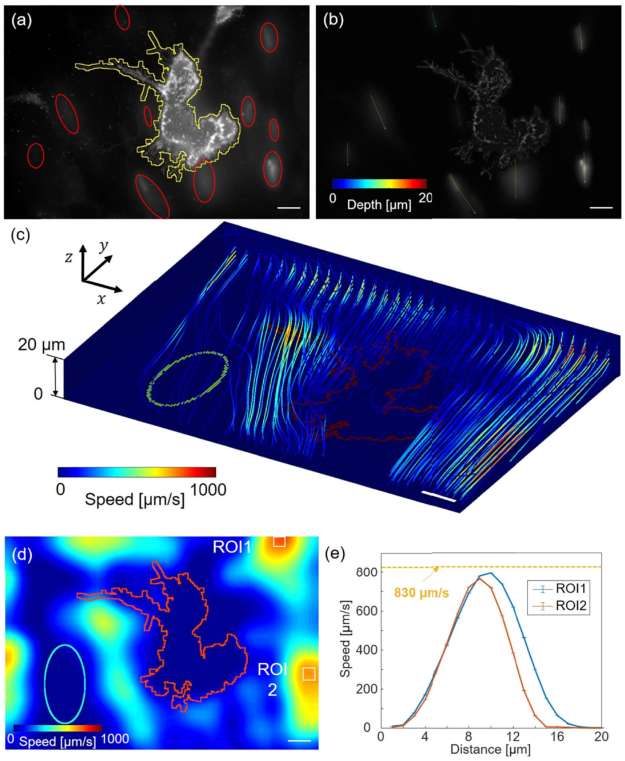

Fig. 6. Analysis of fluid stream obtained with tunable SIM. (a) An example of tunable SIM raw data including U87 cells surrounded by beads flowing in a microfluidic channel. Region is visualized with yellow boundary. Segmented ellipsoidal-shaped beads are depicted in red. (b) Beads flowing at different depths expressed with different colored arrows in reconstructed tunable SIM image. (c) 3D fluid stream lines measured with tunable SIM. The target fluorescent cell is depicted in red. The position of a nonfluorescent cell can be observed and is visualized with a green boundary. (d) Velocity distribution map of a plane 10 μm from the channel floor. (e) Velocity plot for ROI 1 and 2 at different distances from the channel floor. Theoretical maximum flow velocity shown in orange dashed line. Scalebars; 10 μm.

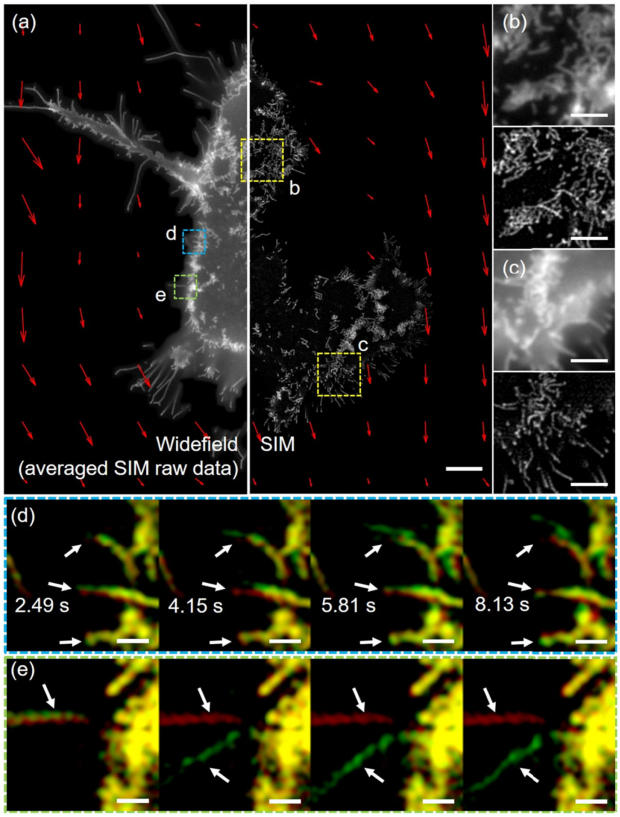

Fig. 7. Visualization of stress induced morphological changes. (a) Comparison of reconstructed tunable SIM and widefield images. The fluid flow is visualized with arrows, indicating the direction and velocity. (b,c) Expanded widefield (upper column) and SIM image (lower column) of the subarea depicted with yellow dashed square in (a). (d,e) Dynamics of actin cytoskeletal structure observed by tunable SIM in the regions marked by the cyan and green dashed squares in (a). Structure at initial time point t_0 is shown in red, while the structure at corresponding time points $t_0 + \Delta t$ are shown in green. Scalebars; 5 μm in (a), 2 μm in (b,c), and 0.5 μm in (d,e).

$\boldsymbol{r}_s$ and $\boldsymbol{r}_d$ regions in a single frame. If we simply neglect information contained in the $\boldsymbol{r}_s$ regions, a single bead flowing through such regions will be segmented and captured in a discontinuous manner. To remove such artifacts, we analyzed beads flowing in $\boldsymbol{r}_s$ regions as well, for cases where the extracted bead flow was located in close vicinity to the boundary between $\boldsymbol{r}_s$ and $\boldsymbol{r}_d$ regions. To extract beads flowing in the $\boldsymbol{r}_s$ regions, the difference between the i-th, and $i + 15$-th images (which have identical orientation and phase SIM illumination) was used. Assuming that slowly moving objects have no significant change between a single tunable SIM image acquisition sequence, only the flowing beads remain in the subtracted image. The information extracted from both $\boldsymbol{r}_s$ and $\boldsymbol{r}_d$ regions were then combined into a single image and used for bead segmentation as shown in Figs. 6(a) and 6(b). (see Fig. S11 of Supplement 1 for more details on bead segmentation).

The instantaneous speed and height was deduced by the size of the major and minor axis of each bead [38,39]. Because the imaging system was focused onto the bottom surface of the cell, we assume that the size of the minor axis corresponded to the height of the beads due to the defocused PSF. Considering the effect of defocus, the size and direction of the major axis and the exposure time of the camera were used to extract the instantaneous flow speed. Based on automatic image segmentation with morphological image processing, we visualized the fluid flow surrounding a target cell of interest [Fig. 6(b)]. Each flowing bead was represented by an arrow where the color corresponds to the depth, and the direction and length correspond to the velocity. Accumulated beads flowing in each frame during a 30 s interval were visualized with streamlines in Fig. 6(c). The outline of the fluorescent U87 cell in the channel was overlaid with a red boundary. At the edge of the FOV, we see the straight laminar flow flowing in the y-axis direction. To check the validity of our measurements, we analyzed the fluid speed distribution for two different regions of interest (ROI) in the laminar flow region [Fig. 6(d)]. The average velocity of the beads follows a parabolic distribution as a function of depth as shown in Fig. 6(e) as we expect from hydrodynamic flow fully developed within the channel [39,40]. However, this distribution is broken near the volume of the cell where we see random direction and velocity of the flow showing the disturbed turbulent flow due to the presence of the cell. Furthermore, we can also deduce the existence of other cells that failed to express fluorescence by observing the shape of the 3D fluid streamlines [Figs. 6(c) and 6(d), Visualization 1].

To understand the effects of shear stress on the cell, we also observed the slower fine dynamics of the actin cytoskeleton structure. Figure 7(a) shows the comparison between conventional widefield and tunable SIM images, overlaid with the average

velocity plot of the surrounding fluid. In conventional widefield imaging, the diffraction-limited resolution as well as the out of focus background prohibits observation of fine structural changes [Figs. 7(a)–7(c)]. Using tunable SIM, we obtained depth sectioned and resolution doubled views of the entire cell without any artifacts due to the rapidly flowing fluorescent beads [Figs. 7(a)–7(e)]. The actin structure at the center of the cell as well as at the apical cell membrane boundaries were all well resolved compared to conventional widefield imaging. By tracing the fluorescent beads around the cell and the subcellular actin structure simultaneously, we succeeded in visualizing 100 nm scale subdiffraction-limited structural changes and the fast dynamics of beads flowing at ∼800 μm/s in a single experimental setup, for the first time to our knowledge. Comparing the images when the microfluidic pressure pump was turned on and off, we clearly saw that the external shear stress had an effect on the movement and reconstruction of the actin cytoskeleton. Interestingly, we observed that the actin structure at the filopodia-like cellular boundary was most responsive to the induced shear stress [Fig. 7(d) and 7(e), Visualization 2].

4. DISCUSSION

In our current demonstration, SIM reconstruction for the $\boldsymbol{r}_s$ regions was carried out using conventional methods simply with the information in the $\boldsymbol{r}_d$ regions removed. However, applying constant reconstruction parameters to the entire image can induce artifacts, due to spatially-varying PSFs in a single image. Recently, research has shown that these artifacts can be removed by splitting the acquired image into several tiles and applying different reconstruction parameters to each tile during the SIM reconstruction process [41]. In tunable SIM, the different parameters can be simply extracted, from each segmented $\boldsymbol{r}_s$ region and applied independently for image reconstruction. Moving forward, tunable SIM can potentially be adapted to apply spatially varying structured illumination patterns during the illumination process as well, that can further compensate spatially varying aberrations.

Although our current work focused on demonstrating the advantage in simultaneous acquisition of conventional widefield and SIM imaging, this is not the sole functionality limited by the system. For example, although high speed cameras that can obtain full pixel resolution images at ∼1000 s of frames per second are commercially available, total measurement time is limited to only a few seconds due to memory bottlenecks. Because DMDs offer refresh rates of up to 20 kHz, our platform can be easily adapted to perform stroboscopic imaging to target regions of the FOV and track dynamics occurring faster than the camera framerate, while imaging other regions at subdiffraction-limited resolutions without an upper limit on the total observation time.

Because the system has no moving parts, it is robust and versatile and can also be expanded to other applications that rely on specific illumination or detection sequences such as optical sectioning SIM [42], total internal reflection microscopy [43], ghost imaging [44], optical tomography [45,46], and Fourier ptychography [47] (see Fig. S12 of Supplement 1 for more details on optical sectioning SIM). By adding the freedom of arbitrary designable illumination across the FOV, our approach may also be used to design custom illumination and detection variables which can potentially enhance the efficiency of computational imaging [48].

5. CONCLUSION

In this work, we proposed a customizable illumination and image acquisition pipeline that can adapt to the characteristics of the samples of interest. Using this pipeline, we demonstrated tunable SIM, a simple imaging system that can obtain spatially varying spatiotemporal resolutions across the FOV. Through experiments, we verified that spatially varying dynamics that could not be measured using SIM or conventional widefield imaging alone could be easily observed using tunable SIM.

The optical characteristics of a microscope with respect to space and time has been traditionally thought to be fixed across the entire FOV. We believe that the present study will facilitate further research that can break this common belief and enable imaging of sophisticated objects that require different imaging characteristics or modalities throughout the FOV.

Funding. National Research Foundation of Korea (2016R1C1B201530, 2017M3C7A1044966, 2019M3E5D2A01063812); TJ Park Foundation.

Disclosures. The authors declare no conflicts of interest.

See Supplement 1 for supporting content.

REFERENCES

1. L. Schermelleh, A. Ferrand, T. Huser, C. Eggeling, M. Sauer, O. Biehlmaier, and G. P. C. Drummen, "Super-resolution microscopy demystified," Nat. Cell Biol. **21**, 72–84 (2019).
2. S. W. Hell, S. J. Sahl, M. Bates, X. Zhuang, R. Heintzmann, M. J. Booth, J. Bewersdorf, G. Shtengel, H. Hess, P. Tinnefeld, A. Honigmann, S. Jakobs, I. Testa, L. Cognet, B. Lounis, H. Ewers, S. J. Davis, C. Eggeling, D. Klenerman, K. I. Willig, G. Vicidomini, M. Castello, A. Diaspro, and T. Cordes, "The 2015 super-resolution microscopy roadmap," J. Phys. D **48**, 443001 (2015).
3. B. Huang, H. Babcock, and X. Zhuang, "Breaking the diffraction barrier: super-resolution imaging of cells," Cell **143**, 1047–1058 (2010).
4. B. Huang, M. Bates, and X. Zhuang, "Super-resolution fluorescence microscopy," Annu. Rev. Biochem. **78**, 993–1016 (2009).
5. A. M. Sydor, K. J. Czymmek, E. M. Puchner, and V. Mennella, "Super-resolution microscopy: from single molecules to supramolecular assemblies," Trends Cell Biol. **25**, 730–748 (2015).
6. E. Betzig, G. H. Patterson, R. Sougrat, O. W. Lindwasser, S. Olenych, J. S. Bonifacino, M. W. Davidson, J. Lippincott-Schwartz, and H. F. Hess, "Imaging intracellular fluorescent proteins at nanometer resolution," Science **313**, 1642–1645 (2006).
7. J. Schnitzbauer, Y. Wang, S. Zhao, M. Bakalar, T. Nuwal, B. Chen, and B. Huang, "Correlation analysis framework for localization-based super-resolution microscopy," Proc. Natl. Acad. Sci. USA **115**, 3219–3224 (2018).
8. S. W. Hell and J. Wichmann, "Breaking the diffraction resolution limit by stimulated emission: stimulated-emission-depletion fluorescence microscopy," Opt. Lett. **19**, 780–782 (1994).
9. G. Vicidomini, P. Bianchini, and A. Diaspro, "STED super-resolved microscopy," Nat. Methods **15**, 173–182 (2018).
10. M. G. L. Gustafsson, "Surpassing the lateral resolution limit by a factor of two using structured illumination microscopy," J. Microsc. **198**, 82–87 (2000).
11. A. Jost and R. Heintzmann, "Superresolution multidimensional imaging with structured illumination microscopy," Annu. Rev. Mater. Res. **43**, 261–282 (2013).
12. J. Demmerle, C. Innocent, A. J. North, G. Ball, M. Muller, E. Miron, A. Matsuda, I. M. Dobbie, Y. Markaki, and L. Schermelleh, "Strategic and practical guidelines for successful structured illumination microscopy," Nat. Protoc. **12**, 988–1010 (2017).

13. R. Heintzmann and C. G. Cremer, "Laterally modulated excitation microscopy: improvement of resolution by using a diffraction grating," Proc. SPIE **3568**, 185–196 (1999).
14. D. Li, L. Shao, B.-C. Chen, X. Zhang, M. Zhang, B. Moses, D. E. Milkie, J. R. Beach, J. A. Hammer, and M. Pasham, "Extended-resolution structured illumination imaging of endocytic and cytoskeletal dynamics," Science **349**, aab3500 (2015).
15. X. Huang, J. Fan, L. Li, H. Liu, R. Wu, Y. Wu, L. Wei, H. Mao, A. Lal, P. Xi, L. Tang, Y. Zhang, Y. Liu, S. Tan, and L. Chen, "Fast, long-term, super-resolution imaging with Hessian structured illumination microscopy," Nat. Biotechnol. **36**, 451–459 (2018).
16. R. Heintzmann and T. Huser, "Super-resolution structured illumination microscopy," Chem. Rev. **117**, 13890–13908 (2017).
17. M. Saxena, G. Eluru, and S. S. Gorthi, "Structured illumination microscopy," Adv. Opt. Photon. **7**, 241–275 (2015).
18. A. Curd, A. Cleasby, K. Makowska, A. York, H. Shroff, and M. Peckham, "Construction of an instant structured illumination microscope," Methods **88**, 37–47 (2015).
19. A. G. York, P. Chandris, D. D. Nogare, J. Head, P. Wawrzusin, R. S. Fischer, A. Chitnis, and H. Shroff, "Instant super-resolution imaging in live cells and embryos via analog image processing," Nat. Methods **10**, 1122–1126 (2013).
20. P. W. Winter, A. G. York, D. D. Nogare, M. Ingaramo, R. Christensen, A. Chitnis, G. H. Patterson, and H. Shroff, "Two-photon instant structured illumination microscopy improves the depth penetration of super-resolution imaging in thick scattering samples," Optica **1**, 181–191 (2014).
21. Y. Guo, D. Li, S. Zhang, Y. Yang, J.-J. Liu, X. Wang, C. Liu, D. E. Milkie, R. P. Moore, and U. S. Tulu, "Visualizing intracellular organelle and cytoskeletal interactions at nanoscale resolution on millisecond timescales," Cell **175**, 1430–1442 (2018).
22. D. Dan, M. Lei, B. Yao, W. Wang, M. Winterhalder, A. Zumbusch, Y. Qi, L. Xia, S. Yan, and Y. Yang, "DMD-based LED-illumination super-resolution and optical sectioning microscopy," Sci. Rep. **3**, 1116 (2013).
23. A. Sandmeyer, M. Lachetta, H. Sandmeyer, W. Hübner, T. Huser, and M. Müller, "DMD-based super-resolution structured illumination microscopy visualizes live cell dynamics at high speed and low cost," bioRxiv 797670 (2019).
24. L. Song, H.-W. Lu-Walther, R. Förster, A. Jost, M. Kielhorn, J. Zhou, and R. Heintzmann, "Fast structured illumination microscopy using rolling shutter cameras," Meas. Sci. Technol. **27**, 055401 (2016).
25. F. Strohl and C. F. Kaminski, "Speed limits of structured illumination microscopy," Opt. Lett. **42**, 2511–2514 (2017).
26. N. Chakrova, A. S. Canton, C. Danelon, S. Stallinga, and B. Rieger, "Adaptive illumination reduces photobleaching in structured illumination microscopy," Biomed. Opt. Express **7**, 4263–4274 (2016).
27. S. Dong, P. Nanda, R. Shiradkar, K. Guo, and G. Zheng, "High-resolution fluorescence imaging via pattern-illuminated Fourier ptychography," Opt. Express **22**, 20856–20870 (2014).
28. R. Forster, K. Wicker, W. Muller, A. Jost, and R. Heintzmann, "Motion artefact detection in structured illumination microscopy for live cell imaging," Opt. Express **24**, 22121–22134 (2016).
29. R. Forster, W. Muller, R. Richter, and R. Heintzmann, "Automated distinction of shearing and distortion artefacts in structured illumination microscopy," Opt. Express **26**, 20680–20694 (2018).
30. J. Fan, X. Huang, L. Li, S. Tan, and L. Chen, "A protocol for structured illumination microscopy with minimal reconstruction artifacts," Biophys. Rep. **5**, 80–90 (2019).
31. S. K. Nayar and V. Branzoi, "Adaptive dynamic range imaging: optical control of pixel exposures over space and time," in *Ninth IEEE International Conference on Computer Vision* (IEEE, 2003), pp. 1168–1175.
32. G. Narita, Y. Watanabe, and M. Ishikawa, "Dynamic projection mapping onto deforming non-rigid surface using deformable dot cluster marker," IEEE Trans. Vis. Comput. Graphics **23**, 1235–1248 (2016).
33. M. Kleiner, D. Brainard, and D. Pelli, "What's new in Psychtoolbox-3?," in Volume 36 of European Conference on Visual Perception (ECVP 2007) Abstract Supplement (SAGE, 2007).
34. J. Dillon, "sharedmatrix" https://www.mathworks.com/matlabcentral/fileexchange/28572-sharedmatrix.
35. M. Muller, V. Monkemoller, S. Hennig, W. Hubner, and T. Huser, "Open-source image reconstruction of super-resolution structured illumination microscopy data in ImageJ," Nat. Commun. **7**, 10980 (2016).
36. A. Markwirth, M. Lachetta, V. Monkemoller, R. Heintzmann, W. Hubner, T. Huser, and M. Muller, "Video-rate multi-color structured illumination microscopy with simultaneous real-time reconstruction," Nat. Commun. **10**, 4315 (2019).
37. Y. Ma, D. Li, Z. J. Smith, D. Li, and K. Chu, "Structured illumination microscopy with interleaved reconstruction (SIMILR)," J. Biophoton. **11**, e201700090 (2018).
38. A. Glia, P. Sukumar, A. Brimmo, M. Deliorman, M. A. Qasaimeh, B. L. Gray, and H. Becker, "Immuno-capture of cells in open microfluidics: microfluidic probes integrated with herringbone micro-mixers," Proc. SPIE **10875**, 108751F (2019).
39. L. Saias, J. Autebert, L. Malaquin, and J.-L. Viovy, "Design, modeling and characterization of microfluidic architectures for high flow rate, small footprint microfluidic systems," Lab Chip **11**, 822–832 (2011).
40. M. H. Winer, A. Ahmadi, and K. C. Cheung, "Application of a three-dimensional (3D) particle tracking method to microfluidic particle focusing," Lab Chip **14**, 1443–1451 (2014).
41. D. P. Hoffman and E. Betzig, "Tiled reconstruction improves structured illumination microscopy," bioRxiv: 2020.2001.2006.895318 (2020).
42. M. A. Neil, R. Juškaitis, and T. Wilson, "Method of obtaining optical sectioning by using structured light in a conventional microscope," Opt. Lett. **22**, 1905–1907 (1997).
43. W. Zong, X. Huang, C. Zhang, T. Yuan, L.-L. Zhu, M. Fan, and L. Chen, "Shadowless-illuminated variable-angle TIRF (siva-TIRF) microscopy for the observation of spatial-temporal dynamics in live cells," Biomed. Opt. Express **5**, 1530–1540 (2014).
44. M. P. Edgar, G. M. Gibson, and M. J. Padgett, "Principles and prospects for single-pixel imaging," Nat. Photonics **13**, 13–20 (2019).
45. J. Sharpe, U. Ahlgren, P. Perry, B. Hill, A. Ross, J. Hecksher-Sørensen, R. Baldock, and D. Davidson, "Optical projection tomography as a tool for 3D microscopy and gene expression studies," Science **296**, 541–545 (2002).
46. W. Choi, C. Fang-Yen, K. Badizadegan, S. Oh, N. Lue, R. R. Dasari, and M. S. Feld, "Tomographic phase microscopy," Nat. Methods **4**, 717–719 (2007).
47. C. Kuang, Y. Ma, R. Zhou, J. Lee, G. Barbastathis, R. R. Dasari, Z. Yaqoob, and P. T. So, "Digital micromirror device-based laser-illumination Fourier ptychographic microscopy," Opt. Express **23**, 26999–27010 (2015).
48. A. Chaware, C. L. Cooke, K. Kim, and R. Horstmeyer, "Towards an intelligent microscope: adaptively learned illumination for optimal sample classification," arXiv:1910.10209 (2019).